

## MODEL DEVELOPMENT FOR ATOMIC FORCE MICROSCOPE STAGE MECHANISMS\*

RALPH C. SMITH<sup>†</sup>, ANDREW G. HATCH<sup>†</sup>, TATHAGATA DE<sup>‡</sup>, MURTI V. SALAPAKA<sup>‡</sup>,  
RICARDO C. H. DEL ROSARIO<sup>§</sup>, AND JULIE K. RAYE<sup>¶</sup>

**Abstract.** In this paper, we develop nonlinear constitutive equations and resulting system models quantifying the nonlinear and hysteretic field-displacement relations inherent to lead zirconate titanate (PZT) devices employed in atomic force microscope stage mechanisms. We focus specifically on PZT rods utilizing  $d_{33}$  motion and PZT shells driven in  $d_{31}$  regimes, but the modeling framework is sufficiently general to accommodate a variety of drive geometries. In the first step of the model development, lattice-level energy relations are combined with stochastic homogenization techniques to construct nonlinear constitutive relations which accommodate the hysteresis inherent to ferroelectric compounds. Second, these constitutive relations are employed in classical rod and shell relations to construct system models appropriate for presently employed nanopositioner designs. The capability of the models for quantifying the frequency-dependent hysteresis inherent to the PZT stages is illustrated through comparison with experimental data.

**Key words.** atomic force microscope, hysteresis model, dynamics

**AMS subject classifications.** 74D10, 74M05

**DOI.** 10.1137/05063307X

**1. Introduction.** Stage mechanisms employing the ferroelectric material lead zirconate titanate (PZT) have played a fundamental role in scanning tunneling microscope (STM) and atomic force microscope (AFM) design since their inception due to the high set point accuracy, large dynamic range, and relatively small temperature sensitivity exhibited by the compounds [14]. To illustrate, consider the prototypical AFM design depicted in Figure 1. To ascertain the three-dimensional (3-D) surface structure of a sample, it is moved laterally along a predetermined  $x$ - $y$  grid by a PZT-driven stage. The response of a highly flexible microcantilever to changing atomic surface forces is monitored by a reflected laser beam measured via a photodiode, and forces corresponding to the cantilever displacement changes are determined via Hooke's law. A feedback law is used to determine voltages to a transverse PZT stage which produces displacements in the  $z$ -direction to maintain constant forces. A complete scan in this manner provides a surface image of the compounds. Additionally, PZT actuators are often used to drive the microcantilevers at resonance to achieve the tapping mode operation used to reduce damage to specimens. The reader is referred

---

\*Received by the editors June 5, 2005; accepted for publication (in revised form) April 24, 2006; published electronically October 3, 2006.

<http://www.siam.org/journals/siap/66-6/63307.html>

<sup>†</sup>Department of Mathematics, Center for Research in Scientific Computation, North Carolina State University, Raleigh, NC 27695 (rsmith@eos.ncsu.edu, aghatch@comcast.net). The research of the first author was supported in part through NSF grant CMS-0099764 and in part by the Air Force Office of Scientific Research through the grants AFOSR-F49620-01-1-0107 and AFOSR-FA9550-04-1-0203. The research of the second author was supported by DARPA subcontract 1000-G-CF980. Both authors were supported by NSF grant CMS-0201560.

<sup>‡</sup>Electrical Engineering Department, Iowa State University, Ames, IA 50011 (tatha@iastate.edu, murti@iastate.edu). The research of these authors was supported by NSF grant CMS-0201560.

<sup>§</sup>Department of Mathematics, University of the Philippines, Diliman, Quezon City 1101 (rcdelros@math.upd.edu.ph).

<sup>¶</sup>Department of Mathematics, Virginia Commonwealth University, Richmond VA 23284 (jkraye@yahoo.com).

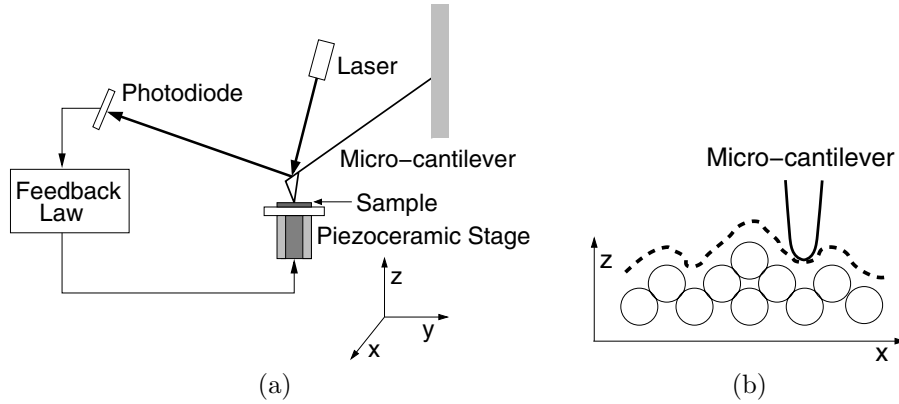


FIG. 1. (a) Configuration of a prototypical AFM, and (b) surface image determined by one lateral sweep.

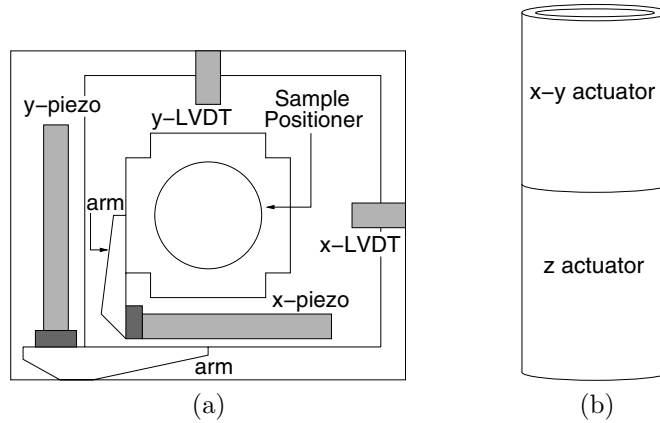


FIG. 2. Actuator configurations employed for sample positioning in AFM: (a) stacked actuators employed as  $x$ - and  $y$ -stages, and (b) cylindrical PZT transducer.

to [11, 13, 14] for additional details regarding AFM applications and design.

Two representative stage designs are depicted in Figure 2. The first employs stacked PZT actuators utilizing  $d_{33}$  electromechanical motion to achieve longitudinal positioning along the prespecified  $x$ - $y$  grid. A second stage provides the transverse motion required to ascertain the sample topography. Rod models with linear and nonlinear electromechanical input relations are constructed to quantify the PZT transducer dynamics in this design. The second geometry employs a cylindrical shell—with half poled  $d_{33}$  to provide horizontal ( $x$ - $y$ ) motion and half poled  $d_{31}$  for vertical ( $z$ ) motion, as depicted in Figure 2(b)—to enhance vibration isolation and reduce hysteresis and constitutive nonlinearities. Thin shell models are developed to characterize this stage design.

To illustrate issues which must be addressed by models, field-displacement data from the stacked actuator depicted in Figure 2(a) is plotted in Figures 3 and 4. The data in Figure 3 was collected at 0.1 Hz and illustrates the nested, hysteretic relation between input fields and generated displacements in a nearly quasi-static regime. The data in Figure 4 was collected at frequencies ranging from 0.279 Hz to 27.9 Hz

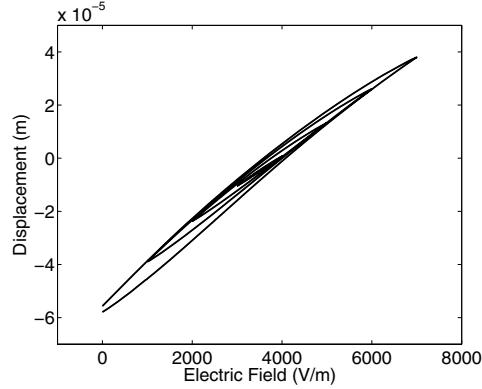


FIG. 3. *Nested minor loops in 0.1 Hz field-displacement data from a stacked PZT stage of the type depicted Figure 2(a).*

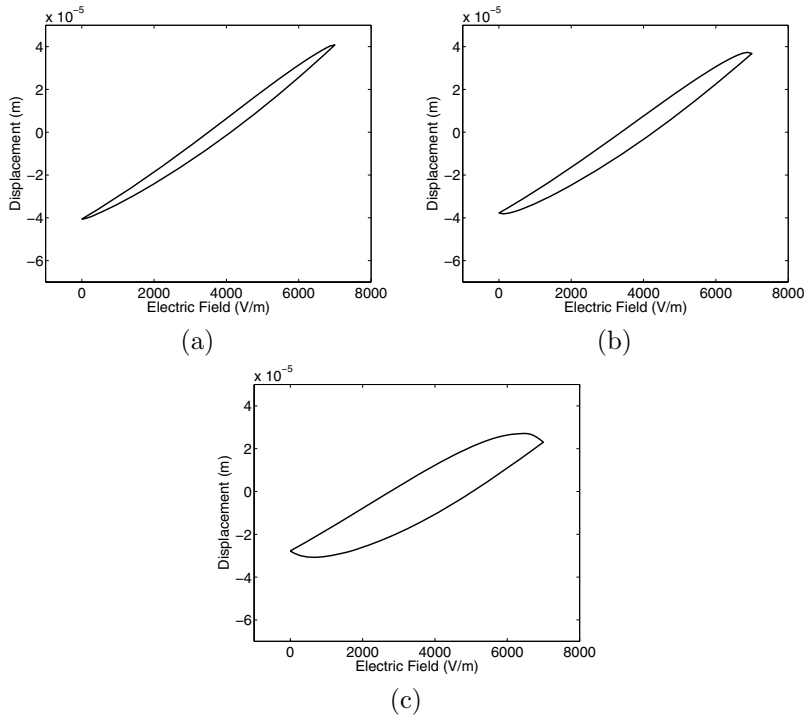


FIG. 4. *Frequency-dependent field-displacement behavior of a stacked PZT stage of the type depicted in Figure 2(a): sample rates of (a) 0.279 Hz, (b) 5.58 Hz, and (c) 27.9 Hz.*

to illustrate the frequency-dependence of the hysteresis as well as certain dynamic effects.

At low frequencies, the inherent hysteresis can be accommodated through proportional-integral-derivative (PID) or robust control designs [7, 8, 22, 29]. However, at the higher frequencies required for applications including real-time monitoring of biological processes (e.g., protein unfolding), comprehensive product diagnostics, and single electron spin detection [28, 40], increasing noise-to-data ratios and diminishing

high-pass characteristics of control filters preclude a sole reliance on feedback laws to eliminate hysteresis.

Alternatively, it is illustrated in [20, 21] that use of charge- or current-controlled amplifiers can essentially eliminate hysteresis. However, this mode of operation can be prohibitively expensive when compared with the more commonly employed voltage-controlled amplifiers, and current control is ineffective if maintaining DC offsets, as is the case when the  $x$ -stage of an AFM is held in a fixed position while a sweep is performed with the  $y$ -stage.

The need to significantly increase scanning speeds with general amplifiers motivates the development of models and model-based control designs which accommodate the frequency-dependent hysteresis inherent to the PZT actuators employed in the AFM stages. As detailed in [30], there exist a number of general approaches and frameworks for quantifying the constitutive nonlinearities and hysteresis in the general class of ferroelectric materials which encompass PZT. These include phenomenological macroscopic models [24], Preisach models [12, 27], domain wall models [33, 34], micromechanical models [6, 18, 19], mesoscopic energy relations [5, 17], and homogenized energy models [32, 39]. Within the context of AFM design, Croft, Shed, and Devasia [7] have employed a combination of a viscoelastic creep model and nonlinear Preisach representation to compensate for hysteresis and creep in an AFM stage, whereas a domain wall model was employed in [35] for the characterization of hysteresis in certain stage constructs. Primary requirements for nonlinear hysteresis models for the PZT actuators in an AFM are (i) flexibility with regard to frequency-dependent hysteresis effects (the frameworks of [7, 35] are limited in this regard), (ii) exact or approximate invertibility for linear control design, and (iii) sufficient efficiency for real-time implementation at the speeds required for present and future applications.

In this paper, we develop AFM transducer models, based on a homogenized energy framework for characterizing hysteresis and constitutive nonlinearities in ferroelectric materials, which meet these criteria. In section 2, we summarize the framework developed in [15, 31, 37, 38, 39] for quantifying hysteresis in the field-polarization relation and develop constitutive equations which characterize the elastic and electromechanical behavior of the PZT material. These constitutive relations are employed in section 3 to construct rod and shell models for the stages depicted in Figure 2, and the well-posedness of the models is established in section 4. Numerical approximation techniques for the transducer models are summarized in section 5, and the capability of the framework to quantify the biased and frequency-dependent hysteresis behavior of the transducers is illustrated in section 6 through a comparison with the experimental data plotted in Figures 2 and 3.

To place this framework in perspective, we briefly summarize the manner in which it compares and contrasts with previous models. As illustrated in [30, 36], the homogenized energy framework provides an energy basis for certain extended Preisach models. However, it also differs in five fundamental ways, and these are detailed in Remark 4 in section 2.4, following the model development. The domain wall model employed in the constitutive relations of [35] is efficient for characterizing hysteresis when inputs are known a priori. As detailed in [30], however, it does not guarantee the closure of biased minor loops in quasi-static regimes, nor does it provide the capability for including frequency-dependent effects due to thermal activation or creep. Hence the present framework, which automatically incorporates these mechanisms, provides significantly more flexibility for the range of operating regimes required for present and future atomic force microscopy applications. Certain preliminary aspects

of the model are presented in [16], which includes the rod model with initial model validation as a prelude for open loop control design. The present work significantly extends that modeling framework through the unified consideration of rod and shell geometries with extensive experimental validation and the presentation of analysis to establish model well-posedness.

The capability of the framework for characterizing frequency-dependent effects, and hence achieving criterion (i), is illustrated in section 6. With regard to criteria (ii) and (iii), the construction and experimental implementation of model inverses to linearize the nonlinear dynamics is demonstrated in [16]. Hence the models provide a framework for characterizing the hysteresis and nonlinear dynamics inherent to PZT-based nanopositioners in a manner which promotes stage and control design.

**2. Constitutive relations.** In this section, we summarize the development of constitutive relations which quantify the nonlinear and hysteretic map between input fields  $E$  and stresses  $\sigma$  and the polarization  $P$  and strains  $\varepsilon$  generated in ferroelectric materials. These relations are developed in three steps. In the first, Helmholtz and Gibbs energy relations are constructed at the lattice level to quantify the *local* dependence of  $P$  and  $\varepsilon$  on  $E$  and  $\sigma$  for regimes in which relaxation due to thermal processes is either negligible or significant. In the second step of the development, material nonhomogeneities, polycrystallinity, and variable field effects are incorporated through the assumption that certain material properties are manifestations of underlying distributions rather than constants. Stochastic homogenization in this manner yields macroscopic models which quantify the bulk hysteretic  $E$ - $P$  behavior measured in ferroelectric materials. Finally, necessary conditions associated with minimization of the Gibbs energy are invoked to obtain 1-D and 2-D constitutive relations quantifying the elastic and electromechanical behavior of the transducer materials.

**2.1. Helmholtz and Gibbs energy relations.** As detailed in [39], an appropriate Helmholtz energy relation is

$$(1) \quad \psi(P, \varepsilon) = \psi_P(P) + \frac{1}{2}Y\varepsilon^2 - a_1\varepsilon P - a_2\varepsilon P^2,$$

where the component

$$\psi_P(P) = \begin{cases} \frac{1}{2}\eta(P + P_R)^2, & P \leq -P_I, \\ \frac{1}{2}\eta(P - P_R)^2, & P \geq P_I, \\ \frac{1}{2}\eta(P_I - P_R) \left( \frac{P^2}{P_I} - P_R \right), & |P| < P_I, \end{cases}$$

quantifies the internal energy due to dipole processes. As shown in Figure 5,  $P_I$  is the positive inflection point that delineates the transition between stable and unstable regions,  $P_0$  denotes the unstable equilibrium, and  $P_R$  is the value of  $P$  at which the positive local minimum of  $\psi$  occurs. The parameter  $\eta$  is the reciprocal of the slope of the  $E$ - $P$  relation after switching occurs. The second term on the right-hand side of (1) quantifies the elastic energy, whereas the third and fourth terms quantify electromechanical coupling effects. Here  $Y$  denotes the Young's modulus, and  $a_1$  and  $a_2$  are electromechanical coupling coefficients.

The Gibbs energy relation

$$(2) \quad G(E, \sigma, P, \varepsilon) = \psi_P(P) + \frac{1}{2}Y\varepsilon^2 - a_1\varepsilon P - a_2\varepsilon P^2 - EP - \sigma\varepsilon$$

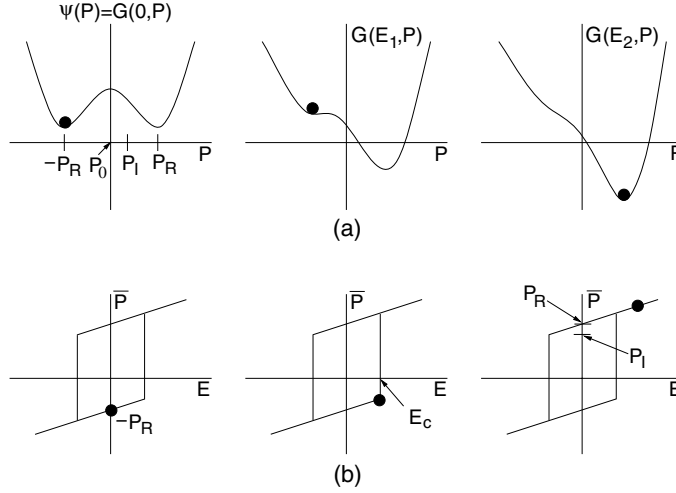


FIG. 5. (a) Helmholtz energy  $\psi$  and Gibbs energy  $G$  for  $\sigma = 0$  and increasing fields  $E$ . (b) Switch in the local polarization  $\bar{P}$  that occurs as  $E$  is increased beyond the local coercive field  $E_c$  given by (4) in the absence of thermal activation.

incorporates the elastic work  $\sigma\varepsilon$  and electromechanical work  $EP$ . This provides the functional that is minimized or balanced with the relative thermal energy to provide local  $E$ - $P$  relations and global electromechanical constitutive equations. The reader is referred to [30, 32] for details regarding the manner in which the Gibbs energy incorporates the dependent variables  $\varepsilon$  and  $P$  in terms of the independent variables  $\sigma$  and  $E$ .

**2.2. Polarization kernel—Negligible thermal activation.** For operating regimes in which relaxation or creep due to thermal processes is negligible, the local  $E$ - $P$  relation is determined from the equilibrium conditions

$$\frac{\partial G}{\partial P} = 0, \quad \frac{\partial^2 G}{\partial P^2} > 0.$$

For the piecewise quadratic functional (2), this yields a polarization kernel of the form

$$(3) \quad \bar{P}(E) = \frac{E}{\eta - 2a_2\varepsilon} + \delta \frac{P_R\eta + \delta a_1\varepsilon}{\eta - 2a_2\varepsilon},$$

where  $\delta = 1$  for positively oriented dipoles and  $\delta = -1$  for those having negative orientation. To specify  $\delta$ , and hence  $\bar{P}$ , in terms of the initial dipole configurations and previous switches, we let  $\delta_0 = \pm 1$  designate the initial dipole orientation and let

$$(4) \quad E_c = \eta(P_R - P_I)$$

define the local coercive field at which the negative well ceases to exist and hence a dipole switch occurs. The local polarization is then given by

$$(5) \quad [\bar{P}(E; E_c, \delta_0)](t) = \begin{cases} \frac{E}{\eta - 2a_2\varepsilon} + \delta_0 \frac{P_R\eta + \delta_0 a_1\varepsilon}{\eta - 2a_2\varepsilon}, & \tau = \emptyset, \\ \frac{E(t) - P_R\eta + a_1\varepsilon}{\eta - 2a_2\varepsilon}, & \tau \neq \emptyset, E(\max \tau) = -E_c, \\ \frac{E(t) + P_R\eta + a_1\varepsilon}{\eta - 2a_2\varepsilon}, & \tau \neq \emptyset, E(\max \tau) = E_c. \end{cases}$$

Here  $\emptyset$  denotes the empty set, and the set of transition times is designated by

$$\tau = \{t \in (0, t_f] \mid E(t) = -E_c \text{ or } E(t) = E_c\},$$

where  $t_f$  denotes the final time under consideration.

*Remark 1.* For the drive levels employed for nanopositioning, the stress effects on the polarization are typically negligible, which motivates taking  $\varepsilon = 0$  in (3) and (5). Hence the relations

$$\overline{P}(E) = \frac{1}{\eta}E + P_R\delta$$

or

$$(6) \quad [\overline{P}(E; E_c, \delta_0)](t) = \begin{cases} \frac{E(t)}{\eta} + P_R\delta_0, & \tau = \emptyset, \\ \frac{E(t)}{\eta} - P_R, & \tau \neq \emptyset, E(\max \tau) = -E_c, \\ \frac{E(t)}{\eta} + P_R, & \tau \neq \emptyset, E(\max \tau) = E_c, \end{cases}$$

are usually employed when characterizing AFM stages.

**2.3. Polarization kernel—Thermal activation.** If thermal relaxation or creep is significant, the Gibbs energy  $G$  and relative thermal energy  $kT/V$  are balanced through the Boltzmann relation

$$(7) \quad \mu(G) = Ce^{-GV/kT}.$$

Here  $k$  is Boltzmann's constant,  $V$  denotes a reference volume chosen to ensure physical relaxation behavior, and  $C$  is chosen to ensure integration to unity for the complete set of admissible inputs. As detailed in [30, 39], this yields the local polarization relation

$$(8) \quad \overline{P} = x_+ \langle P_+ \rangle + x_- \langle P_- \rangle.$$

The fractions  $x_+$  and  $x_-$  of positively and negatively oriented dipoles are quantified by the differential equations

$$\begin{aligned} \dot{x}_+ &= -p_{+-}x_+ + p_{-+}x_-, \\ \dot{x}_- &= -p_{-+}x_- + p_{+-}x_+, \end{aligned}$$

which can be simplified to

$$\dot{x}_+ = -p_{+-}x_+ + p_{-+}(1 - x_+)$$

through the identity

$$\dot{x}_+ + \dot{x}_- = 1.$$

The expected polarizations due to positively and negatively oriented dipoles are

$$(9) \quad \langle P_+ \rangle = \frac{\int_{P_I}^{\infty} P e^{-G(E,P)V/kT} dP}{\int_{P_I}^{\infty} e^{-G(E,P)V/kT} dP}, \quad \langle P_- \rangle = \frac{\int_{-\infty}^{-P_I} P e^{-G(E,P)V/kT} dP}{\int_{-\infty}^{-P_I} e^{-G(E,P)V/kT} dP},$$

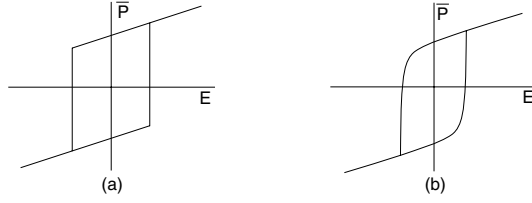


FIG. 6. Hysteron provided by (a) the relation (6) with negligible thermal relaxation, and (b) the relation (8), which incorporates relaxation mechanisms.

where the denominator results from the evaluation of  $C$  in (7). The likelihoods of switching from positive to negative, and conversely, are given by

$$(10) \quad p_{+-} = \frac{1}{\mathcal{T}(T)} \frac{\int_{P_I-\epsilon}^{P_I} e^{-G(E,P)V/kT} dP}{\int_{P_I-\epsilon}^{\infty} e^{-G(E,P)V/kT} dP}, \quad p_{-+} = \frac{1}{\mathcal{T}(T)} \frac{\int_{-P_I}^{-P_I+\epsilon} e^{-G(E,P)V/kT} dP}{\int_{-\infty}^{-P_I+\epsilon} e^{-G(E,P)V/kT} dP},$$

where  $\epsilon$  is taken to be a small positive constant. The relaxation time  $\mathcal{T}$  is the reciprocal of the frequency at which dipoles attempt to switch. It is proven in [30, 39] that  $\bar{P}$  given by (8) converges to the local polarization (6) in the limit  $kT/V \rightarrow 0$  of negligible thermal activation.

*Remark 2.* When constructing the expected polarization relations (9) and likelihoods (10), we use the notation  $G(E, P)$  to indicate that we take  $\varepsilon = \sigma = 0$  in (2) in accordance with the assumption that stress effects on the polarization are negligible at the drive levels employed in AFM stages. This approximation is employed only when defining the stress-independent polarization, and the full expression (2) is employed when constructing elastic constitutive relations in section 2.5.

**2.4. Macroscopic polarization model.** The local polarization relations (6) and (8) exhibit the behavior depicted in Figure 6 and provide reasonable characterization of the  $E$ - $P$  behavior of certain single crystal compounds. However, to incorporate the effects of material and stress nonhomogeneities, polycrystallinity, and variable effective fields  $E_e = E + E_I$ , we assume that the interaction field  $E_I$  and local coercive field  $E_c$  given by (4) are manifestations of underlying distributions rather than constants. If we designate the associated densities by  $\nu_1$  and  $\nu_2$ , the macroscopic field-polarization behavior is quantified by the relation

$$(11) \quad [P(E)](t) = \int_0^\infty \int_{-\infty}^\infty \nu_1(E_c) \nu_2(E_I) [\bar{P}(E + E_I; E_c, \xi)](t) dE_I dE_c,$$

where the kernel  $\bar{P}$  is given by (6) or (8).

As detailed in [30, 32], the densities  $\nu_1$  and  $\nu_2$  are assumed to satisfy the physical criteria

$$(12) \quad \begin{aligned} (i) \quad & \nu_1(x) \text{ defined for } x > 0, \\ (ii) \quad & \nu_2(-x) = \nu_2(x), \\ (iii) \quad & |\nu_1(x)| \leq c_1 e^{-a_1 x}, \\ & |\nu_2(x)| \leq c_2 e^{-a_2 |x|} \end{aligned}$$



for positive  $c_1, a_1, c_2, a_2$ . The restricted domain in (i) reflects the fact that the coercive field  $E_c$  is positive, whereas the symmetry enforced in the interaction field through (ii) yields the symmetry observed in low-field Rayleigh loops. Hypothesis (iii) incorporates the physical observation that the coercive and interaction fields decay as a function of distance, and guarantees that integration against the piecewise linear kernel yields finite polarization values.

**2.4.1. Model implementation.** Approximation of (11) through Gaussian quadrature techniques yields the approximate relation

$$(13) \quad [P(E)](t) = \sum_{i=1}^{N_i} \sum_{j=1}^{N_j} \nu_1(E_{c_i}) \nu_2(E_{I_j}) [\bar{P}(E_{I_j} + E; E_{c_i}, \xi_j)](t) v_i w_j,$$

where  $E_{I_j}, E_{c_i}$  denote the abscissas associated with respective quadrature formulae and  $v_i, w_j$  are the respective weights—e.g., see [30]. Highly efficient algorithms for implementing the approximate polarization model (13) with the kernel (6) for the case of negligible thermal activation can be found in [30, 39]. Algorithms for implementing the model with the thermally active kernel (8) are presented in [4]. MATLAB code for both cases can be accessed at the website <http://www.siam.org/books/fr32> associated with [30].

**2.4.2. Density estimation.** Techniques for identifying the densities  $\nu_1$  and  $\nu_2$  are illustrated in [30, 32]. For certain applications, reasonable accuracy is provided by a priori functions satisfying the physical criteria (12) and having a small number of parameters to be estimated through least squares fits to data—e.g., variances and means in normal and lognormal relations. For more general applications requiring high accuracy for a wide range of operating conditions, the  $N_i + N_j$  discretized density values  $\nu_1(E_{c_i})$  and  $\nu_2(E_{I_j})$  can be estimated through the least squares techniques detailed in [30, 32].

*Remark 3.* From the perspective of both numerical and experimental implementation and the establishment of the well-posedness of resulting transducer models, it is important to quantify the regularity between input fields and the polarization predicted by (11). In the appendix, it is established that  $P$  given by (11) is continuous with respect to  $E$ .

*Remark 4.* The formulation of the model as a superposition of kernels bears some resemblance to Preisach models, and it is illustrated in [30, 36] that the framework provides an energy basis for certain extended Preisach formulations. However, the energy framework differs from the classical Preisach model, characterized by the properties of deletion and congruency, in five aspects which prove crucial for actuator characterization and model-based control design. (i) For certain density choices, parameters can be correlated with attributes of the data to facilitate model construction and updating. (ii) The incorporation of relative thermal energy provides the thermal activation mechanisms required to characterize relaxation and creep. (iii) Stress and temperature-dependencies (e.g., see [1, 26]) are incorporated into the kernel rather than weights, as is the case for Preisach models, which eliminates the necessity of vector-valued lookup tables. (iv) Derivation of the kernels using Ising theory yields hysterons which accommodate measured noncongruencies and avoids the input or output-dependent densities associated with Preisach models. (v) The framework automatically incorporates low-field reversible behavior without the extensions required by Preisach theory.

**2.5. Constitutive relations.** To obtain elastic constitutive relations, the equilibrium condition

$$\frac{\partial G}{\partial \varepsilon} = 0$$

is invoked to obtain

$$\sigma = Y\varepsilon - a_1 P - a_2 P^2,$$

which reduces to Hooke's law when  $P = 0$ . To incorporate internal damping, we posit that in the absence of electromechanical effects, stress is proportional to a linear combination of strain and strain rate (the Kelvin–Voigt damping hypothesis). Finally, we note that the PZT stage mechanisms are poled and hence operate about the remanence polarization  $P = P_R$  rather than the depoled state  $P = 0$ . (The remanence polarization is that which remains when the applied field is reduced to zero following positive saturation.) When combined with the polarization model (11), this yields the 1-D constitutive relations

$$(14) \quad \begin{aligned} \sigma &= Y\varepsilon + C\dot{\varepsilon} - a_1(P - P_R) - a_2(P - P_R)^2, \\ [P(E)](t) &= \int_0^\infty \int_{-\infty}^\infty \nu_1(E_c)\nu_2(E_I)[\bar{P}(E + E_I; E_c, \xi)](t) dE_I dE_c, \end{aligned}$$

where  $C$  is the Kelvin–Voigt damping coefficient. These relations are employed when constructing rod models to characterize the hysteretic dynamics shown in Figures 3 and 4 for the stacked actuators employed in the stage construction depicted in Figure 2(a).

The constitutive behavior of the PZT shell depicted in Figure 2(b) differs from that of the rod in two fundamental aspects: (i) the longitudinal actuation is due to  $d_{31}$  rather than  $d_{33}$  electromechanical coupling mechanisms and (ii) longitudinal and circumferential stresses and strains are coupled due to the curvature. To designate the coupled material behavior, we let  $\varepsilon_x, \sigma_x$  and  $\varepsilon_\theta, \sigma_\theta$  denote the normal strains and stresses in the longitudinal and circumferential directions, respectively, and we denote shear strains and stresses by  $\varepsilon_{x\theta}$  and  $\sigma_{x\theta}$ . Finally, we let  $\nu$  denote the Poisson ratio for the material. The resulting 2-D constitutive relations

$$(15) \quad \begin{aligned} \sigma_x &= \frac{Y}{1-\nu^2}(\varepsilon_x + \nu\varepsilon_\theta) + \frac{C}{1-\nu^2}(\dot{\varepsilon}_x + \nu\dot{\varepsilon}_\theta) - \frac{1}{1-\nu} [a_1(P - P_R) + a_2(P - P_R)^2], \\ \sigma_\theta &= \frac{Y}{1-\nu^2}(\varepsilon_\theta + \nu\varepsilon_x) + \frac{C}{1-\nu^2}(\dot{\varepsilon}_\theta + \nu\dot{\varepsilon}_x) - \frac{1}{1-\nu} [a_1(P - P_R) + a_2(P - P_R)^2], \\ \sigma_{x\theta} &= \frac{Y}{2(1+\nu)}\varepsilon_{x\theta} + \frac{C}{2(1+\nu)}\dot{\varepsilon}_{x\theta}, \\ [P(E)](t) &= \int_0^\infty \int_{-\infty}^\infty \nu_1(E_c)\nu_2(E_I)[\bar{P}(E + E_I; E_c, \xi)](t) dE_I dE_c \end{aligned}$$

are employed when constructing transducer models for cylindrical nanopositioning stages.

**3. Transducer models for stacked and cylindrical AFM stages.** We now employ the 1-D constitutive relation (14) and 2-D relation (15) to construct models for the stacked and cylindrical AFM stages depicted in Figure 2. For the stacked actuator, we consider two frameworks: (i) a distributed PDE model, which quantifies displacements along the rod length as a function of the input field, and (ii) a lumped model, which exploits the assumption of uniform stresses and fields along the rod length to motivate an ODE quantifying displacements only at the rod end. A comparison between characterization capabilities provided by the two frameworks is provided in section 6. For the cylindrical shell design, we summarize a Donnell–Mushtari model which quantifies vertical motion provided by the  $z$ -component of the stage depicted in Figure 2(b).

### 3.1. Rod model for the stacked actuator.

**3.1.1. Distributed rod model.** We consider first the development of a distributed rod model which quantifies the displacement  $u(t, x)$  along the rod length. In accordance with present stage design, one end of the rod is assumed fixed, while the other encounters resistance due to the connecting mechanisms, as depicted in Figure 7. We assume that this latter contribution can be modeled as a damped elastic system with mass  $m_\ell$ , stiffness  $k_\ell$ , and damping coefficient  $c_\ell$ . The density, cross-sectional area, and length of the rod are denoted by  $\rho$ ,  $A$ , and  $\ell$ , and, in accordance with (14), the Young’s modulus and Kelvin–Voigt damping parameter are denoted by  $Y$  and  $C$ .

Force balancing yields the relation

$$(16) \quad \rho A \frac{\partial^2 u}{\partial t^2} = \frac{\partial N}{\partial x},$$

where the resultant  $N = \int_A \sigma dA$  is given by

$$N = Y A \frac{\partial u}{\partial x} + C A \frac{\partial^2 u}{\partial x \partial t} - a_1 [P(E) - P_R] - a_2 [P(E) - P_R]^2,$$

once the linear relation  $\varepsilon = \frac{\partial u}{\partial x}$  is employed for the strains in (14). The nonlinear and hysteretic map between input fields  $E$  and the polarization  $P$  is specified by (11). The fixed-end condition yields  $u(t, 0) = 0$ , and balancing forces at  $x = \ell$  yields the energy dissipating end condition

$$N(t, \ell) = -k_\ell u(t, \ell) - c_\ell \frac{\partial u}{\partial t}(t, \ell) - m_\ell \frac{\partial^2 u}{\partial t^2}(t, \ell).$$

Finally, initial conditions are taken to be  $u(0, x) = u_0(x)$  and  $\frac{\partial u}{\partial t}(0, x) = u_1(x)$ . This provides a strong formulation of the stacked actuator model.

To define a weak or variational form of the model which is appropriate for well-posedness analysis, approximation, or control design, states  $z = (u(\cdot), u(\ell))$  are con-

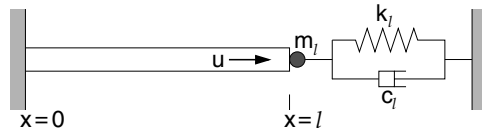


FIG. 7. Rod of length  $\ell$  and cross-sectional area  $A$  with a fixed end at  $x = 0$  and energy dissipating boundary conditions at  $x = \ell$ .

sidered in the state space  $X = L^2(0, \ell) \times \mathbb{R}$  with the inner product

$$(17) \quad \langle \Phi_1, \Phi_2 \rangle_X = \int_0^\ell \rho A \phi_1 \phi_2 dx + m_\ell \varphi_1 \varphi_2,$$

where  $\Phi_1 = (\phi_1, \varphi_1)$ ,  $\Phi_2 = (\phi_2, \varphi_2)$  with  $\varphi_1 = \phi_1(\ell)$ ,  $\varphi_2 = \phi_2(\ell)$ . The space of test functions is taken to be

$$V = \{ \Phi = (\phi, \varphi) \in X \mid \phi \in H^1(0, \ell), \phi(0) = 0, \phi(\ell) = \varphi \}$$

with the inner product

$$(18) \quad \langle \Phi_1, \Phi_2 \rangle_V = \int_0^\ell Y A \phi_1' \phi_2' dx + k_\ell \varphi_1 \varphi_2.$$

Multiplication by  $\phi \in H_0^1(0, \ell) = \{ \phi \in H^1(0, \ell) \mid \phi(0) = 0 \}$  and integration by parts in space yields the weak model formulation

$$(19) \quad \begin{aligned} & \int_0^\ell \rho A \frac{\partial^2 u}{\partial t^2} \phi dx + \int_0^\ell \left[ Y A \frac{\partial u}{\partial x} + C A \frac{\partial^2 u}{\partial x \partial t} \right] \frac{d\phi}{dx} dx \\ &= \int_0^\ell f \phi dx + A [a_1(P - P_R) + a_2(P - P_R)^2] \int_0^\ell \frac{d\phi}{dx} dx \\ & \quad - \left[ k_\ell u(t, \ell) + c_\ell \frac{\partial u}{\partial t}(t, \ell) + m_\ell \frac{\partial^2 u}{\partial t^2}(t, \ell) \right] \phi(\ell), \end{aligned}$$

which must be satisfied for all  $\phi \in V$ .

**3.1.2. Lumped rod model.** The assumption that fields and stresses are uniform along the rod length motivates the conclusion that strains (relative displacements) also exhibit negligible  $x$ -dependence. Since the position of the sample is dictated by the position of the rod tip at  $x = \ell$ , this motivates the development of a lumped model which quantifies  $u_\ell(t) = u(t, \ell)$ .

From the assumption of uniform strains along the rod length, we take

$$\varepsilon(t) = \frac{u_\ell(t)}{\ell}$$

in (14). Balancing the forces  $\sigma A$  for the rod with those of the restoring mechanism yields the lumped model

$$\begin{aligned} \rho A \ell \frac{d^2 u_\ell}{dt^2}(t) + \frac{CA}{\ell} \frac{du_\ell}{dt}(t) + \frac{YA}{\ell} u_\ell(t) &= -m_\ell \frac{d^2 u_\ell}{dt^2}(t) - c_\ell \frac{du_\ell}{dt}(t) - k u_\ell(t) \\ &+ A a_1 [P(E(t)) - P_R] + A a_2 [P(E(t)) - P_R]^2 \end{aligned}$$

or, equivalently,

$$(20) \quad m \frac{d^2 u_\ell}{dt^2}(t) + c \frac{du_\ell}{dt}(t) + k u_\ell(t) = \tilde{a}_1 [P(E(t)) - P_R] + \tilde{a}_2 [P(E(t)) - P_R]^2,$$

where

$$(21) \quad m = \rho A \ell + m_\ell, \quad c = \frac{CA}{\ell} + c_\ell, \quad k = \frac{YA}{\ell} + k_\ell, \quad \tilde{a}_1 = A a_1, \quad \tilde{a}_2 = A a_2,$$

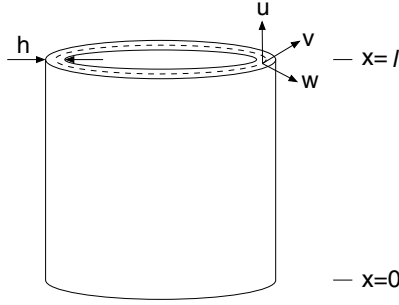


FIG. 8. Orientation of the shell geometry used when quantifying the longitudinal, circumferential, and transverse displacements  $u$ ,  $v$ , and  $w$ .

and the initial conditions are  $u_\ell(0) = u_0$  and  $\frac{du_\ell}{dt}(0) = u_1$ . The polarization  $P$  is specified by the model (11) or discretized model (13).

The model can also be written as the first-order system

$$(22) \quad \begin{aligned} \dot{\vec{u}}_\ell(t) &= A\vec{u}_\ell(t) + \vec{\mathcal{P}}(E(t)), \\ \vec{u}_\ell(0) &= \vec{u}_0, \end{aligned}$$

where  $\vec{u}_\ell(t) = [u_\ell(t), \dot{u}_\ell(t)]^T$ ,  $\vec{u}_\ell(0) = [u_0, u_1]^T$  and

$$A = \begin{bmatrix} 0 & 1 \\ -k/m & -c/m \end{bmatrix},$$

$$\vec{\mathcal{P}}(E(t)) = \frac{1}{m} [\tilde{a}_1(P(E(t)) - P_R) + \tilde{a}_2(P(E(t)) - P_R)^2] \begin{bmatrix} 0 \\ 1 \end{bmatrix}.$$

**3.2. Cylindrical shell model.** To quantify the dynamics of the cylindrical stage depicted in Figure 2(b), we construct a linear shell model with nonlinear inputs quantified by the 2-D constitutive relation (15). We focus on the actuator employed for transverse displacements since real-time control of this component is required to maintain constant forces between the sample and microcantilever. The mass of the shell employed for horizontal translation is combined with the mass of the sample to provide an inertial force acting on the free end of the vertical actuator.

For modeling purposes, we assume that the shell has length  $\ell$ , thickness  $h$ , and radius  $R$ . The axial direction is specified along the  $x$ -axis, and the longitudinal, circumferential, and transverse displacements are respectively denoted by  $u$ ,  $v$ , and  $w$ , as depicted in Figure 8. The density is designated by  $\rho$ , and the region occupied by the reference or middle surface of the shell is specified by  $\Gamma_0 = [0, \ell] \times [0, 2\pi]$ . In accordance with the constitutive relations (15),  $Y$ ,  $C$ , and  $\nu$  denote the Young's modulus, Kelvin-Voigt damping coefficient, and Poisson ratio for the material. We point out that  $\varepsilon_x, \varepsilon_\theta$ , and  $\varepsilon_{x\theta}$  in (15) denote strains at points throughout the shell thickness, whereas 2-D shell models are formulated in terms of strains  $e_x, e_\theta$ , and  $e_{x\theta}$  in the reference surface of the shell. The relationship between the two is established through the assumption that displacements are linear through the shell thickness, which comprises one of the fundamental tenets of linear shell theory [3, 30].

We consider the case in which the bottom edge of the shell ( $x = 0$ ) is clamped and the opposite end ( $x = \ell$ ) is acted upon only by the inertial force associated with the combined mass  $m$  of the  $x$ - $y$  actuator and the sample.

As detailed in [3, 30], force and moment balancing yield the Donnell–Mushtari shell equations

$$\begin{aligned}
 (23) \quad & R\rho h \frac{\partial^2 u}{\partial t^2} - R \frac{\partial N_x}{\partial x} - \frac{\partial N_{x\theta}}{\partial \theta} = 0, \\
 & R\rho h \frac{\partial^2 v}{\partial t^2} - \frac{\partial N_\theta}{\partial \theta} - R \frac{\partial N_{x\theta}}{\partial x} = 0, \\
 & R\rho h \frac{\partial^2 w}{\partial t^2} - R \frac{\partial^2 M_x}{\partial x^2} - \frac{1}{R} \frac{\partial^2 M_\theta}{\partial \theta^2} - 2 \frac{M_{x\theta}}{\partial x \partial \theta} + N_\theta = 0,
 \end{aligned}$$

where the force and moment resultants are

$$\begin{aligned}
 (24) \quad & N_x = \frac{Yh}{1-\nu^2} (e_x + \nu e_\theta) + \frac{Ch}{1-\nu^2} (\dot{e}_x + \nu \dot{e}_\theta) - \frac{h}{1-\nu} [a_1(P - P_R) + a_2(P - P_R)^2], \\
 & N_\theta = \frac{Yh}{1-\nu^2} (e_\theta + \nu e_x) + \frac{Ch}{1-\nu^2} (\dot{e}_\theta + \nu \dot{e}_x) - \frac{h}{1-\nu} [a_1(P - P_R) + a_2(P - P_R)^2], \\
 & N_{x\theta} = \frac{Yh}{2(1+\nu)} e_{x\theta} + \frac{Ch}{2(1+\nu)} \dot{e}_{x\theta}
 \end{aligned}$$

and

$$\begin{aligned}
 (25) \quad & M_x = \frac{Yh^3}{12(1-\nu^2)} (\kappa_x + \nu \kappa_\theta) + \frac{Ch^3}{12(1-\nu^2)} (\dot{\kappa}_x + \nu \dot{\kappa}_\theta), \\
 & M_\theta = \frac{Yh^3}{12(1-\nu^2)} (\kappa_\theta + \nu \kappa_x) + \frac{Ch^3}{12(1-\nu^2)} (\dot{\kappa}_\theta + \nu \dot{\kappa}_x), \\
 & M_{x\theta} = \frac{Yh^3}{24(1+\nu)} \kappa_{x\theta} + \frac{Ch^3}{24(1+\nu)} \dot{\kappa}_{x\theta}.
 \end{aligned}$$

The midsurface strains and changes in curvature are

$$\begin{aligned}
 (26) \quad & e_x = \frac{\partial u}{\partial x}, \quad e_\theta = \frac{1}{R} \frac{\partial v}{\partial \theta} + \frac{w}{R}, \quad e_{x\theta} = \frac{\partial v}{\partial x} + \frac{1}{R} \frac{\partial u}{\partial \theta}, \\
 & \kappa_x = -\frac{\partial^2 w}{\partial x^2}, \quad \kappa_\theta = -\frac{1}{R^2} \frac{\partial^2 w}{\partial \theta^2}, \quad \kappa_{x\theta} = -\frac{2}{R} \frac{\partial^2 w}{\partial x \partial \theta}.
 \end{aligned}$$

The boundary conditions for the fixed-end at  $x = 0$  are taken to be

$$u = v = w = \frac{\partial w}{\partial x} = 0,$$

whereas the conditions

$$\begin{aligned}
 & N_x = -m \frac{\partial^2 u}{\partial t^2}, \quad N_{x\theta} + \frac{M_{x\theta}}{R} = 0, \\
 & Q_x + \frac{1}{R} \frac{\partial M_{x\theta}}{\partial \theta} = 0, \quad M_x = 0,
 \end{aligned}$$

are employed at  $x = \ell$ . The first resultant condition incorporates the inertial force due to the mass  $m$  of the PZT actuator employed for  $x$ - $y$  translation along with the mass of the sample.

To reduce smoothness requirements for approximation and eliminate the Dirac behavior of external inputs at  $x = \ell$ , we also consider a weak formulation of the model. The state is taken to be  $z = (u(\cdot, \cdot), v(\cdot, \cdot), w(\cdot, \cdot), u(\ell, \cdot))$  in the state space

$$X = L^2(\Omega) \times L^2(\Omega) \times L^2(\Omega) \times L^2(0, 2\pi),$$

where

$$\Omega = [0, \ell] \times [0, 2\pi]$$

denotes the shell region. The space of test functions is specified as

$$V = \{ \Phi = (\phi_1, \phi_2, \phi_3, \eta) \in X \mid \phi_1 \in H_0^1(\Omega), \phi_2 \in H_0^1(\Omega), \phi_3 \in H_0^2(\Omega) \},$$

where  $\eta(\theta) = \phi_1(\ell, \theta)$  and

$$(27) \quad \begin{aligned} H_0^1(\Omega) &= \{ \phi \in H^1(\Omega) \mid \phi(0, \theta) = 0 \}, \\ H_0^2(\Omega) &= \{ \phi \in H^2(\Omega) \mid \phi(0, \theta) = \phi'(0, \theta) = 0 \}. \end{aligned}$$

Through either variation principles—e.g., see [3]—or integration by parts, one obtains the weak formulation of the thin shell model,

$$(28) \quad \begin{aligned} &\int_{\Omega} \left\{ R\rho h \frac{\partial^2 u}{\partial t^2} \phi_1 + RN_x \frac{\partial \phi_1}{\partial x} + N_{x\theta} \frac{\partial \phi_1}{\partial \theta} \right\} d\omega = 0, \\ &\int_{\Omega} \left\{ R\rho h \frac{\partial^2 v}{\partial t^2} \phi_2 + N_{\theta} \frac{\partial \phi_2}{\partial \theta} + RN_{x\theta} \frac{\partial \phi_2}{\partial x} \right\} d\omega = 0, \\ &\int_{\Omega} \left\{ R\rho h \frac{\partial^2 w}{\partial t^2} \phi_3 - RM_x \frac{\partial^2 \phi_3}{\partial x^2} - 2M_{x\theta} \frac{\partial^2 \phi_3}{\partial x \partial \theta} - \frac{1}{R} M_{\theta} \frac{\partial^2 \phi_3}{\partial \theta^2} + N_{\theta} \phi_3 \right\} d\omega = 0, \end{aligned}$$

which must be satisfied for all  $\Phi \in V$ . The resultants are given by (24) and (25) with midsurface strains and changes in curvature designated in (26).

*Remark 5.* It is noted that the  $d_{31}$  poling, used to generate vertical motion in the stage, produces no polarization contributions to the moments. However, transverse displacements  $w$  in the shell model are generated by the  $N_{\theta}$  resultant in the  $w$  relation, and hence all three components of the displacement are coupled.

**3.3. Frequency-dependent dynamics.** One of the requirements of the nanopositioner models is the capability to characterize the frequency-dependent behavior shown in Figure 2. This behavior is due to a combination of dielectric losses, thermal relaxation processes, and elastic and damping properties, and it is incorporated in the framework in two places. The dielectric losses and relaxation behavior are incorporated through the balance of the Gibbs and relative thermal energies via the Boltzmann relation (7) and subsequent average polarization relations (9) and likelihood expressions (10). Hence this component of the polarization model incorporates the property that dipole dynamics can lag behind field dynamics as frequencies are increased. Dynamics associated with inertial, elastic, and internal damping properties of the actuators are incorporated through the force balances (16) and (23) and resultant definitions. In combination, this provides the framework with significant flexibility regarding a range of dynamics operating regimes.

#### 4. Model well-posedness.

**4.1. Rod model.** To provide a framework which facilitates the establishment of criteria that guarantee the existence of a unique solution to the distributed rod model with nonlinear inputs, we consider a Hilbert space formulation of the weak model formulation (19) with the state and test function spaces

$$X = L^2(0, \ell) \times \mathbb{R},$$

$$V = \{\Phi = (\phi, \varphi) \in X \mid \phi \in H^1(0, \ell), \phi(0) = 0, \phi(\ell) = \varphi\}$$

and inner products

$$(29) \quad \begin{aligned} \langle \Phi_1, \Phi_2 \rangle_X &= \int_0^\ell \rho A \phi_1 \phi_2 dx + m_\ell \varphi_1 \varphi_2, \\ \langle \Phi_1, \Phi_2 \rangle_V &= \int_0^\ell Y A \phi_1' \phi_2' dx + k_\ell \varphi_1 \varphi_2, \end{aligned}$$

where  $\Phi_1 = (\phi_1, \varphi_1)$ ,  $\Phi_2 = (\phi_2, \varphi_2)$  with  $\varphi_1 = \phi_1(\ell)$ ,  $\varphi_2 = \phi_2(\ell)$ .

It is observed that  $V$  is densely and continuously embedded in  $X$  with  $|\Phi|_X \leq c|\Phi|_V$ ; this is expressed by  $V \hookrightarrow X$ . Moreover, when one defines conjugate dual spaces  $X^*$  and  $V^*$ —e.g.,  $V^*$  denotes the linear space of all conjugate linear continuous functionals on  $V$ —two observations are important: (i)  $X^*$  can be identified with  $X$  through the Riesz map and (ii)  $X^* \hookrightarrow V^*$ . Hence the two spaces comprise what is termed a Gelfand triple,  $V \hookrightarrow X \cong X^* \hookrightarrow V^*$  with pivot space  $X$  and duality pairing (duality product)  $\langle \cdot, \cdot \rangle_{V^*, V}$ . The latter is defined as the extension by continuity of the inner product  $\langle \cdot, \cdot \rangle_X$  from  $V \times X$  to  $V^* \times X$ . Hence elements  $v^* \in V^*$  have the representation  $v^*(v) = \langle v^*, v \rangle_{V^*, V}$ .

We now define the stiffness and damping sesquilinear forms  $\sigma_i : V \times V \rightarrow \mathbb{C}$ ,  $i = 1, 2$ , by

$$(30) \quad \begin{aligned} \sigma_1(\Phi_1, \Phi_2) &= \langle \Phi_1, \Phi_2 \rangle_V, \\ \sigma_2(\Phi_1, \Phi_2) &= \int_0^\ell C A \phi_1' \phi_2' dx + c_\ell \varphi_1 \varphi_2. \end{aligned}$$

It can be directly verified that the stiffness form satisfies

$$(H1) \quad |\sigma_1(\Phi_1, \Phi_2)| \leq c_1 |\Phi_1|_V |\Phi_2|_V \text{ for some } c_1 \in \mathbb{R} \quad (\text{bounded}),$$

$$(H2) \quad \operatorname{Re} \sigma_1(\Phi_1, \Phi_1) \geq c_2 |\Phi_1|_V^2 \text{ for some } c_2 > 0 \quad (V\text{-elliptic}),$$

$$(H3) \quad \sigma_1(\Phi_1, \Phi_2) = \overline{\sigma_1(\Phi_2, \Phi_1)} \quad (\text{symmetric}),$$

for all  $\psi, \phi \in V$ . Moreover, the damping term  $\sigma_2$  satisfies

$$(31) \quad (H4) \quad |\sigma_2(\Phi_1, \Phi_2)| \leq c_3 |\Phi_1|_V |\Phi_2|_V \text{ for some } c_3 \in \mathbb{R} \quad (\text{bounded}),$$

$$(H5) \quad \operatorname{Re} \sigma_2(\Phi_1, \Phi_1) \geq c_4 |\Phi_1|_V^2 \text{ for some } c_4 > 0 \quad (V\text{-elliptic}).$$

The input space is taken to be the Hilbert space  $U = \mathbb{R}$ , and the input operator  $B : U \rightarrow V^*$  is defined by

$$(32) \quad \langle [B(E)](t), \Phi \rangle_{V^*, V} = [a_1(P(E(t)) - P_R) + a_2(P(E(t)) - P_R)^2] \int_0^\ell \phi' dx$$



for  $\Phi = (\phi, \varphi)$  with  $\varphi = \phi(\ell)$ . It is observed that  $B$  can be expressed as

$$(33) \quad [B(E)](t) = [b(E)](t) \cdot g, \quad g \in V^*,$$

where

$$(34) \quad \begin{aligned} [b(E)](t) &= (P(E(t)) - P_R) + a_2(P(E(t)) - P_R)^2, \\ g(\Phi) &= \int_0^\ell \phi' dx. \end{aligned}$$

The model (19) can then be written in the abstract weak formulation

$$(35) \quad \begin{aligned} \langle \ddot{u}(t), \Phi \rangle_{V^*, V} + \sigma_2(\dot{u}(t), \Phi) + \sigma_1(u(t), \Phi) &= \langle [B(E)](t), \Phi \rangle_{V^*, V}, \\ u(0) &= u_0, \quad \dot{u}(0) = u_1, \end{aligned}$$

for all  $\Phi \in V$ .

Alternatively, one can define the operators  $A_i \in \mathcal{L}(V, V^*)$ ,  $i = 1, 2$ , by

$$(36) \quad \langle A_i \Phi_1, \Phi_2 \rangle_{V^*, V} = \sigma_i(\Phi_1, \Phi_2)$$

and formulate the model in operator form as

$$(37) \quad \begin{aligned} \ddot{u}(t) + A_2 \dot{u}(t) + A_1 u(t) &= [B(E)](t), \\ u(0) &= u_0, \quad \dot{u}(0) = u_1, \end{aligned}$$

in the dual space  $V^*$ . This formulation illustrates the analogy between the infinite-dimensional, strongly damped elastic model and the familiar finite-dimensional relations (22).

**4.1.1. Model well-posedness.** As a prelude to establishing the well-posedness of the beam model with hysteretic  $E$ - $P$  relations, we provide a lemma which quantifies the smoothness of the input operator.

LEMMA 1. *Consider field inputs  $E \in C[0, T]$ . The input operator  $B$  defined by (32) then satisfies*

$$(38) \quad B(E) \in L^2(0, T; V^*).$$

*Proof.* In the appendix, we establish that for continuous input fields  $E$  the polarization satisfies  $P \in C[0, T]$ , which implies that  $b$  defined by (34) satisfies  $b(\cdot) : C[0, T] \rightarrow C[0, T]$ . Hence the norm

$$\|[B(E)](t)\|_{V^*} = \sup_{v \in V} \frac{|[b(E)](t) \cdot g(v)|}{\|v\|_V}$$

exists for each  $t \in [0, T]$ . Since  $\|[B(E)](t)\|_{V^*} = |[b(E)](t)| \cdot \|g\|_{V^*}$ , it follows that

$$\|B(E)\|_{L^2(0, T; V^*)}^2 \leq \max_{t \in [0, T]} \{|[b(E)](t)|^2\} \cdot T \cdot \|g\|_{V^*}^2,$$

which implies that

$$B(E) \in L^2(0, T; V^*). \quad \square$$

The well-posedness of the model is established by the following theorem, whose proof follows directly from Theorem 4.1 of [3] or Theorem 2.1 and Remark 2.1 of [2].

**THEOREM 2.** *Let  $\sigma_1$  and  $\sigma_2$  be given by (30), and consider continuous field inputs  $E \in C[0, T]$ . There then exists a unique solution  $w$  to (35), or equivalently (37), which satisfies*

$$\begin{aligned} u &\in C(0, T; V), \\ \dot{u} &\in C(0, T; X). \end{aligned}$$

**4.2. Shell model.** Similar well-posedness results can be obtained for the shell model (28) through consideration of an analogous Hilbert space formulation of the model. Details regarding the construction of appropriate inner product spaces, sesquilinear forms, and operators can be found in [30, 35].

**5. Numerical approximation techniques.** To implement the distributed models for either the rectangular stacked actuator or the cylindrical actuator, it is necessary to develop appropriate approximation techniques to discretize the modeling PDE. To accomplish this, we consider general Galerkin methods in which basis functions are comprised of spline or spline-Fourier tensor products. The resulting methods can accommodate a variety of boundary conditions, are sufficiently accurate to resolve fine-scale dynamics, and can be employed for constructing reduced-order proper orthogonal decomposition approximates for real-time implementation.

**5.1. Stacked actuator model.** To approximate the weak form of the stacked actuator model (19), we employ a finite element discretization and a finite difference discretization in time. The semidiscrete system resulting from the finite element approximation is appropriate for finite-dimensional continuous time control design, whereas the fully discrete system is amenable to simulations and control implementation.

To obtain a semidiscrete system, we consider a uniform partition of  $[0, \ell]$  with points  $x_j = jh$ ,  $j = 0, 1, \dots, N$ , with step size  $h = \ell/N$ , where  $N$  denotes the number of subintervals. The spatial basis  $\{\phi_j\}_{j=1}^N$  is then comprised of linear splines

$$\begin{aligned} \phi_j(x) &= \frac{1}{h} \begin{cases} (x - x_{j-1}), & x_{j-1} \leq x < x_j, \\ (x_{j+1} - x), & x_j \leq x \leq x_{j+1}, \\ 0, & \text{otherwise,} \end{cases} \quad i = 1, \dots, N-1, \\ \phi_N(x) &= \frac{1}{h} \begin{cases} (x - x_{N-1}), & x_{N-1} \leq x \leq x_N, \\ 0, & \text{otherwise} \end{cases} \end{aligned}$$

(see [25] for details regarding the convergence analysis for the method). The solution  $u(t, x)$  to (19) is subsequently approximated by the expansion

$$u^N(t, x) = \sum_{j=1}^N u_j(t) \phi_j(x).$$

Through construction, the approximate solution satisfies the essential boundary condition  $u^N(t, 0) = 0$  and can attain arbitrary displacements at  $x = \ell$ .

The projection of the problem (19) onto the finite-dimensional subspace  $V^N$  yields the semidiscrete system

$$(39) \quad \begin{aligned} \dot{\mathbf{z}}(t) &= \mathbb{A} \mathbf{z}(t) + A [a_1(P(t) - P_R) + a_2(P(t) - P_R)^2] \mathbf{B}, \\ \mathbf{z}(0) &= \mathbf{z}_0, \end{aligned}$$

where  $\mathbf{z}(t) = [u_1(t), \dots, u_N(t), \dot{u}_1(t), \dots, \dot{u}_N(t)]^T$  and

$$(40) \quad \mathbb{A} = \begin{bmatrix} 0 & \mathbb{I} \\ -\mathbb{M}^{-1}\mathbb{K} & -\mathbb{M}^{-1}\mathbb{Q} \end{bmatrix}, \quad \mathbf{B} = \begin{bmatrix} 0 \\ \mathbb{M}^{-1}\mathbf{b} \end{bmatrix}.$$

The mass, stiffness, and damping matrices have the components

$$\begin{aligned} [\mathbb{M}]_{ij} &= \begin{cases} \int_0^\ell \rho A \phi_i \phi_j dx, & i \neq N \text{ or } j \neq N, \\ \int_0^\ell \rho A \phi_i \phi_j dx + m_\ell, & i = N \text{ and } j = N, \end{cases} \\ [\mathbb{K}]_{ij} &= \begin{cases} \int_0^\ell Y A \phi'_i \phi'_j dx, & i \neq N \text{ or } j \neq N, \\ \int_0^\ell Y A \phi'_i \phi'_j dx + k_\ell, & i = N \text{ and } j = N, \end{cases} \end{aligned}$$

and

$$[\mathbb{Q}]_{ij} = \begin{cases} \int_0^\ell c A \phi'_i \phi'_j dx, & i \neq N \text{ or } j \neq N, \\ \int_0^\ell c A \phi'_i \phi'_j dx + c_\ell, & i = N \text{ and } j = N, \end{cases}$$

and the force vector is defined by

$$[\mathbf{b}]_i = \int_0^\ell \phi'_i dx.$$

The system (39) can be employed for finite-dimensional control design. For subsequent implementation, we consider a temporal discretization of (39) using a modified trapezoid rule. For temporal stepsizes  $\Delta t$ , this yields the difference equation

$$(41) \quad \mathbf{z}_{k+1} = \mathbb{W} \mathbf{z}_k + \frac{1}{2} \left[ a_1 \tilde{P}(t_k) + a_1 \tilde{P}(t_{k+1}) + a_2 \tilde{P}^2(t_k) + a_2 \tilde{P}^2(t_{k+1}) \right] \mathbb{V} \mathbf{B},$$

where  $\tilde{P} = P - P_R$ ,  $t_j = j\Delta t$ ,  $\mathbf{z}_j$  approximates  $\mathbf{z}(t_j)$ , and

$$\mathbb{W} = \left( \mathbb{I} - \frac{\Delta t}{2} \mathbb{A} \right)^{-1} \left( \mathbb{I} + \frac{\Delta t}{2} \mathbb{A} \right), \quad \mathbb{V} = \Delta t \left( \mathbb{I} - \frac{\Delta t}{2} \mathbb{A} \right)^{-1}.$$

This yields an A-stable method requiring moderate storage and providing moderate accuracy.

**5.2. Cylindrical actuator model.** Due to the inherent coupling between longitudinal, circumferential, and transverse displacements in combination with the 2-D support of the middle surface, the numerical approximation of the model for the cylindrical actuator is significantly more complicated than the approximation of the stacked actuator model. Among the issues which must be addressed when constructing finite element or general Galerkin methods for the shell is the choice of elements which avoid shear and membrane locking and the maintenance of boundary conditions. We summarize here a spline-based Galerkin method developed in [9] for thin shells and direct the reader to that source for details regarding the construction of constituent matrices and convergence properties of the method. Details regarding the use of this approximation method for LQR (linear quadratic regulator) control of shells utilizing PZT actuators can be found in [10].

The bases for the  $u$ ,  $v$ , and  $w$  displacements are respectively taken to be

$$\Phi_{u_k}(\theta, x) = e^{im\theta} \phi_{u_n}(x), \quad \Phi_{v_k}(\theta, x) = e^{im\theta} \phi_{v_n}(x), \quad \Phi_{w_k}(\theta, x) = e^{im\theta} \phi_{w_n}(x),$$

where  $\phi_{u_n}$ ,  $\phi_{v_n}$ , and  $\phi_{w_n}$  are cubic  $B$ -splines modified to satisfy the boundary conditions (e.g., see p. 79 of [25]). The approximating subspaces are

$$V_u^N = \text{span} \{ \Phi_{u_k} \}_{k=1}^{N_u}, \quad V_v^N = \text{span} \{ \Phi_{v_k} \}_{k=1}^{N_v}, \quad V_w^N = \text{span} \{ \Phi_{w_k} \}_{k=1}^{N_w},$$

and the approximate displacements are represented by the expansions

$$\begin{aligned} u^N(t, \theta, x) &= \sum_{k=1}^{N_u} u_k(t) \Phi_{u_k}(\theta, x), \\ v^N(t, \theta, x) &= \sum_{k=1}^{N_v} v_k(t) \Phi_{v_k}(\theta, x), \\ w^N(t, \theta, x) &= \sum_{k=1}^{N_w} w_k(t) \Phi_{w_k}(\theta, x). \end{aligned} \tag{42}$$

The restriction of the problem (28) to the approximating subspaces and construction of the forcing vectors subsequently yields the matrix system

$$\begin{aligned} \dot{\mathbf{z}}^N(t) &= \mathbb{A} \mathbf{z}(t) + [a_1(P(t) - P_R) + a_2(P(t) - P_R)^2] \mathbf{B}, \\ \mathbf{z}(0) &= \mathbf{z}_0, \end{aligned} \tag{43}$$

where  $\mathbf{z} = [\boldsymbol{\vartheta}(t), \dot{\boldsymbol{\vartheta}}(t)]^T$ , with  $\boldsymbol{\vartheta}(t) = [\mathbf{u}(t), \mathbf{v}(t), \mathbf{w}(t)]^T$ , and

$$\mathbb{A} = \begin{bmatrix} 0 & \mathbb{I} \\ -\mathbb{M}^{-1}\mathbb{K} & -\mathbb{M}^{-1}\mathbb{Q} \end{bmatrix}, \quad \mathbf{B} = \begin{bmatrix} 0 \\ \mathbb{M}^{-1}\mathbf{b} \end{bmatrix}.$$

The reader is referred to [9, 30] for details concerning the construction of the mass, stiffness, and damping matrices  $\mathbb{M}$ ,  $\mathbb{K}$ , and  $\mathbb{Q}$ .

## 6. Model validation.

**6.1. Characterization of the stacked actuator.** We consider the capability of the modeling framework for characterizing the dynamics of the stacked actuator depicted in Figure 2(a). The PZT actuator had a length of  $\ell = 2 \times 10^{-2}$  m and a

TABLE 1

*Parameters employed in the distributed (PDE) model (19) and lumped (ODE) model (20) for the stacked actuator.*

Distributed model					
Parameter	$\rho$	$Y$	$C$	$m_\ell$	
value	7600	$7 \times 10^{10}$	$5 \times 10^6$	4.015	
Parameter	$k_\ell$	$c_\ell$	$a_1$	$a_2$	
value	$8.49 \times 10^{-5}$	440	$1.54 \times 10^{11}$	0	
Lumped model					
Parameter	$m$	$k$	$c$	$\tilde{a}_1$	$\tilde{a}_2$
value	4.21	$8.75 \times 10^7$	$1.52 \times 10^5$	$8.75 \times 10^7$	0

square cross-sectional face of width  $w = 5 \times 10^{-3}$  m, so that the cross-sectional area is  $A = 2.5 \times 10^{-5}$  m<sup>2</sup>. As illustrated in Figure 7, one end of the actuator was considered fixed, whereas the other encountered elastic, damping, and inertial effects due to the attached components of the stage mechanism.

To validate and illustrate properties of the models, we consider three regimes: (i) end displacements quantified by the lumped model (20) with the thermally inactive kernel (6) employed in the polarization model (14), (ii) displacements characterized by the lumped model with the thermally active polarization kernel (8), and (iii) end displacements quantified by the discretization (41) of the distributed model (19). It is illustrated that whereas the latter choice incorporates the distributed rod nature of the device, the fact that fields and stresses are uniform along the rod length implies that relative displacements are also uniform. A comparison of the ODE and PDE model predictions at the rod tip ( $x = \ell$ ) illustrates that, as a result, the ODE provides a highly accurate characterization with significantly less computation cost. Hence the ODE model is advantageous for real-time experimental implementation.

The construction of the models requires the estimation of elastic, damping, and electromechanical parameters in addition to identification of the densities  $\nu_1$  and  $\nu_2$ . The densities were estimated through least squares fits to the data using the techniques detailed in [30, 32]. The manufacturer specifications  $\rho = 7600$  kg/m<sup>3</sup> and  $Y = 7 \times 10^{10}$  N/m<sup>2</sup> were employed for the density and Young's modulus, and remaining parameters were estimated through a least squares fit to the data. The resulting values are summarized in Table 1. The relation between the rod and spring parameters is provided by (21).

#### 6.1.1. Lumped model—No thermal activation in polarization relation.

We consider first the characterization of the biased minor loop data shown in Figure 3 and frequency-dependent data from Figure 4 using the lumped model (20) with the thermally inactive kernel (6) employed in the polarization model (14). It should be noted that the stage was disassembled between the quasi-static biased minor loop experiments and the frequency-dependent experiments, which necessitated the re-identification of densities for the two cases.

In the first set of experiments, displacement data measured with an LVDT (linear variable differential transformer) was collected at a sample rate of 0.1 Hz and four input field levels to generate a set of biased and nested transducer responses ranging from nearly linear to hysteretic and nonlinear, as shown in Figures 3 and 9. The densities  $\nu_1$  and  $\nu_2$  and parameters summarized in Table 1 were obtained through a least squares fit to the full data set comprised of four loops. The resulting model accurately quantifies both the nest behavior and the hysteresis measured at increasing

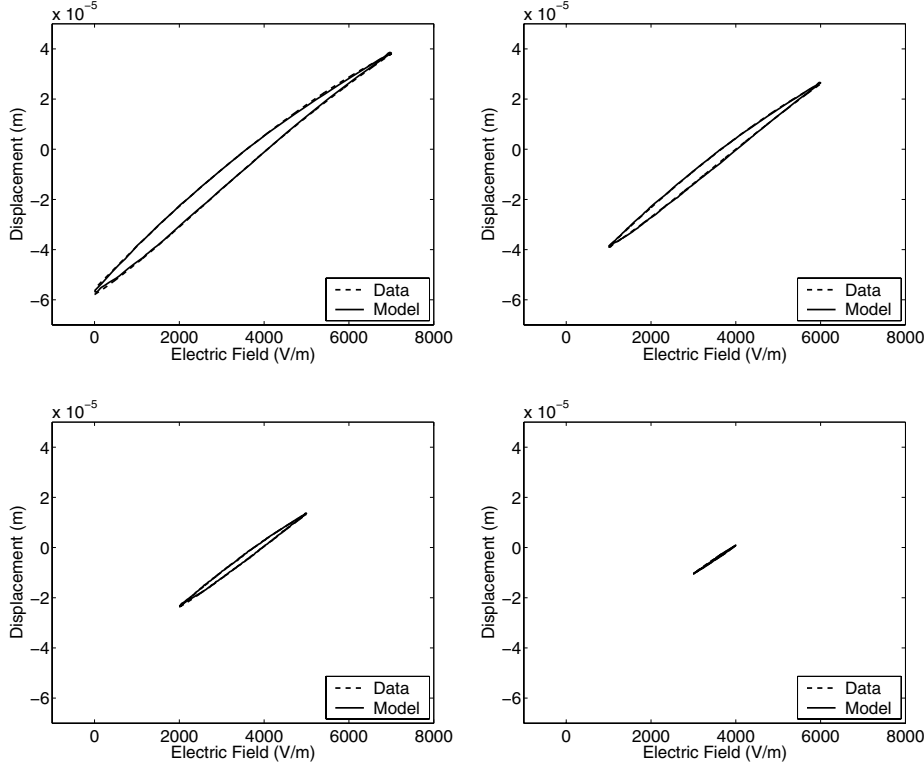


FIG. 9. Characterization of AFM field-displacement behavior at 0.1 Hz using the ODE model (20) with the thermally inactive kernel (6).

input levels.

In a second set of experiments, data was collected at frequencies ranging from 0.279 Hz to 27.9 Hz, yielding the behavior shown in Figure 4. These experiments took longer (approximately 30 minutes), which led to slight heating and accompanying changes in the material constitutive behavior. To accommodate these operating conditions, the data from four frequencies was used to reidentify parameters in the polarization model, thus yielding the fits shown in Figure 10. It is observed that the model characterizes the augmented hysteresis arising at higher frequencies but slightly overpredicts the increase in displacement following field reversal that is due primarily to inertial effects.

**6.1.2. Lumped model—Thermal activation in polarization relation.** We next employ the thermally active kernel (8) in the polarization model to incorporate relaxation effects. Parameters in the polarization model were again identified through a least squares fit to the four frequency data sets, thus yielding the model fit shown in Figure 11. It is observed that use of this more general kernel provides additional accuracy at higher frequencies. Whereas this improves characterization capabilities, the added accuracy comes at the cost of decreased efficiency, and the criteria of accuracy versus efficiency must be balanced when employing the model for real-time control design, as discussed in [16]. We note that use of the thermally active kernel (8) is required when characterizing the creep measured when one actuator is held fixed while a sweep is performed with the other.

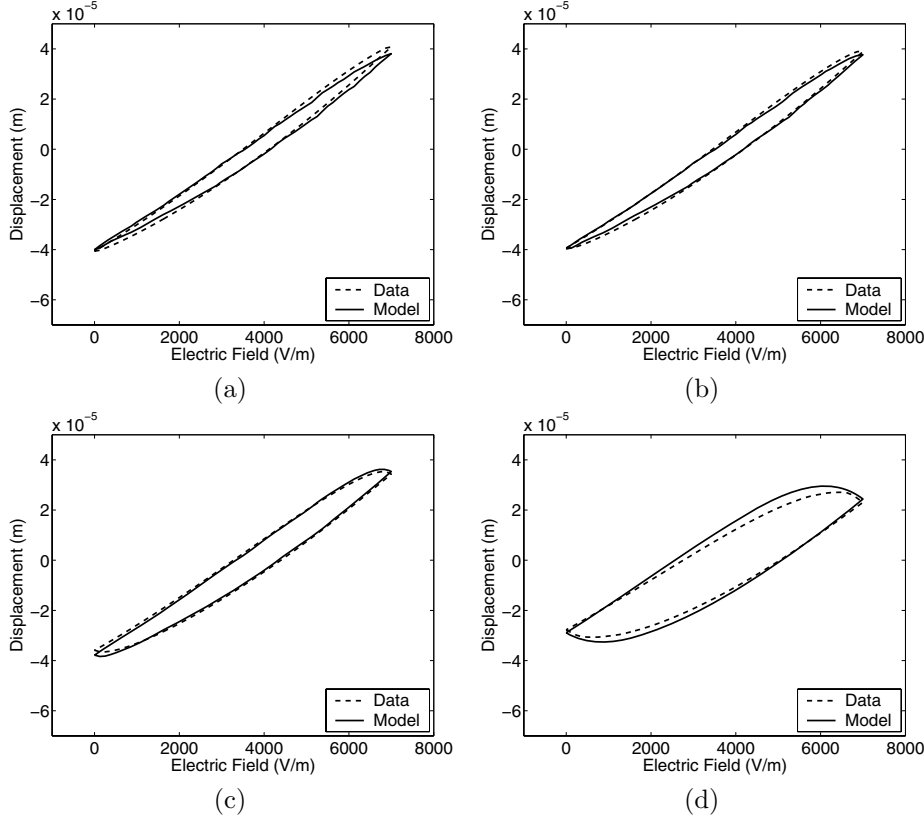


FIG. 10. Characterization of AFM field-displacement behavior using the ODE model (20) with the thermally inactive kernel (6), with sample rates of (a) 0.279 Hz, (b) 1.12 Hz, (c) 5.58 Hz, and (d) 27.9 Hz.

**6.1.3. Lumped model versus distributed model.** It has been observed that whereas quantification of the physics of the stacked actuator leads to the rod model (19), the fact that stresses and fields are uniform along the rod length implies that relative displacements will also be uniform. This motivates consideration of the lumped model (20), which yielded the fits shown in Figures 10 and 11.

To illustrate the validity of this assumption, the difference between the displacement  $u(t, \ell)$ , given by the discretization (41) of (19) with  $N = 16$  basis functions, and the displacement  $u_\ell(t)$ , resulting from (20), is plotted in Figure 12. We emphasize that when constructing the PDE model we employed the parameter values summarized in Table 1, which are *consistent* with the spring parameters due to the relation (21). The maximal difference of  $5 \times 10^{-10}$  is five orders of magnitude less than the micron-level displacements being characterized, thus verifying the validity of the ODE model in this regime. The accuracy of the ODE model has important ramifications for control design since the discretized ODE model is significantly more efficient to implement than the discretized PDE model.

**6.2. Characterization of the shell actuator.** We discuss here the performance of the cylindrical shell model detailed in section 3.2, when discretized using the Galerkin techniques summarized in section 5.2, for characterizing the longitudinal

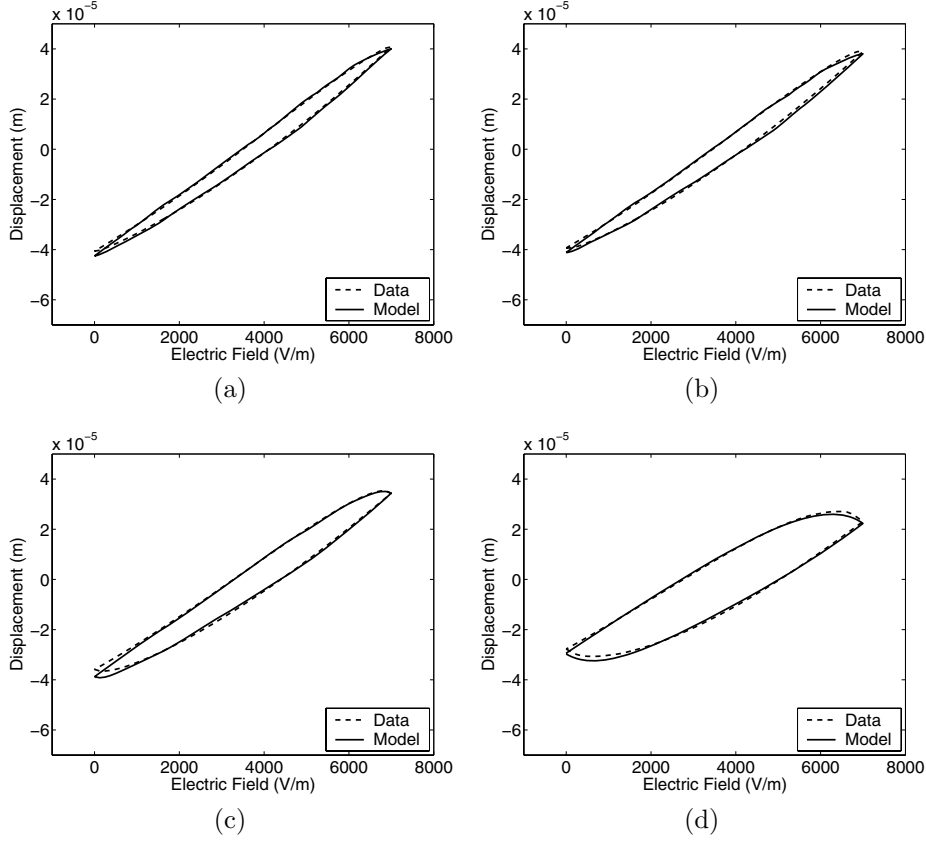


FIG. 11. Characterization of AFM field-displacement behavior using the ODE model (20) with the thermally active kernel (8), with sample rates of (a) 0.279 Hz, (b) 1.12 Hz, (c) 5.58 Hz, and (d) 27.9 Hz.

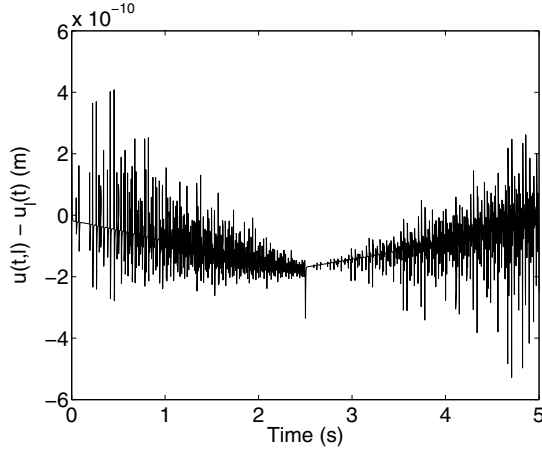


FIG. 12. Difference between the displacement  $u(t, \ell)$  given by the distributed model (19) and  $u_\ell(t)$  given by the lumped model (20).



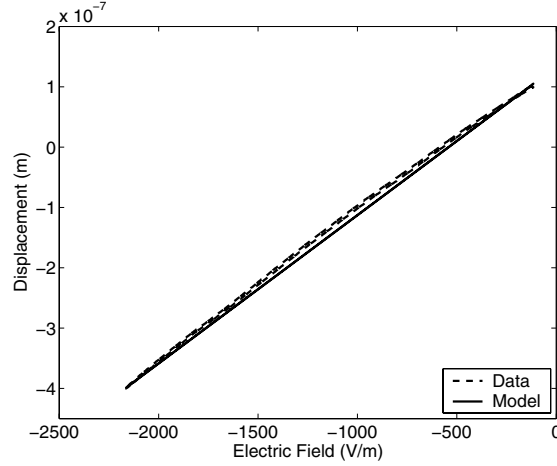


FIG. 13. Characterization of the relation between the field and longitudinal displacements for the cylindrical actuator depicted in Figures 2(b) and 7.

displacements of the cylindrical PZT shell transducer depicted in Figures 2(b) and 7. Whereas the cylindrical PZT elements employed in this design are more complex than the rod elements used in the stage design depicted in Figure 2(a), the overall transducer is simpler and has the advantage of enhanced vibration isolation and diminished hysteresis.

The experimental cylindrical transducer had a length of  $\ell = 0.0396$  m, radius of  $R = 0.0056$  m, and thickness of  $h = 0.0015$  m. The manufacturer specifications  $\rho = 7600$  kg/m<sup>3</sup> and  $Y = 7.1 \times 10^{10}$  N/m<sup>2</sup> were employed for the density and Young's modulus, and remaining model parameters were estimated through a least squares fit to the data.

The longitudinal displacement  $u^N$  provided by (42) is compared in Figure 13 with experimental data collected under quasi-static operating conditions. We note that due to the inherent coupling between the longitudinal, circumferential, and transverse displacements,  $u$ ,  $v$ , and  $w$  in the model (23), the approximate displacements (42) are also coupled and all are obtained through solution of (43)—we plot only  $u^N$  since it corresponds to measured data. For this operating regime, the dynamics were resolved with eight cubic B-splines in  $x$  and seven Fourier elements in  $\theta$ , so  $N_u = N_v = N_w = 56$ .

The nearly linear behavior of the data reflects the low drive levels under consideration. The accurate fit provided by the model illustrates the property that the hysteretic  $E$ - $P$  model (11) yields approximately linear behavior in low drive regimes. The fidelity of the model further illustrates the accuracy and flexibility of the modeling framework.

**7. Concluding remarks.** This characterization framework quantifies both the approximately linear and hysteretic properties of the PZT device employed in AFM positioning mechanisms. In the first step of the development, constitutive relations are constructed through a combination of energy analysis at the lattice level and stochastic homogenization techniques based on the assumption that certain parameters are manifestations of underlying distributions. These relations quantify the frequency-dependent hysteresis exhibited by the materials for general drive regimes

while reducing to approximately linear behavior at low drive regimes. In the second step of the development, these constitutive relations are used to construct lumped and distributed rod and shell models for the various PZT transducer geometries. The accuracy of the models is illustrated through comparison with experimental data from AFM stages.

An important property of the framework is the fact that resulting models can be approximately inverted with nearly the same efficiency as the forward models [16]. This provides a framework with the capability for providing inverse compensators for linear control design [22, 23]. The implementation of feedback control designs for high-speed scanning, using these model-based compensators, is under present investigation.

For either linear control designs employing model inverses or model-based non-linear control designs, it is crucial that discretized models be implementable in real-time. For the stacked actuator model, discretization limits are sufficiently small (e.g.,  $2N = 32$  for the first-order system) to permit efficient implementation with present hardware. Furthermore, it was demonstrated that lumped models provide sufficient accuracy for the considered architecture. The behavior of the shell transducer is significantly more complex due to the coupling between longitudinal, circumferential and transverse displacements, and the construction of reduced-order models based on proper orthogonal decomposition (POD) techniques is under investigation.

**Appendix. Continuity of the polarization model.** We establish here the continuity of the homogenized energy model (11),

$$(44) \quad [P(E)](t) = \int_0^\infty \int_{-\infty}^\infty [\bar{P}(E + E_I; E_c, \xi)](t) \nu_1(E_c) \nu_2(E_I) dE_I dE_c,$$

as a function of both field and time in the case of negligible thermal activation. The densities  $\nu_1$  and  $\nu_2$  satisfy the conditions (12), and the kernel  $\bar{P}$  has the form

$$\bar{P}(E) = \frac{E}{\eta} + P_R \delta(E; E_c, E_I)$$

specified in (6).

We first note that there are at most three values at which  $\delta$  can change sign:  $-E_c$ ,  $E_c$ , and  $-E_c \leq E_T \leq E_c$ . The third is determined by the initial dipole distribution  $\xi$ , as depicted in Figure 14(a), and is typically chosen so that  $E_T = 0$  when  $E + E_I = 0$ .

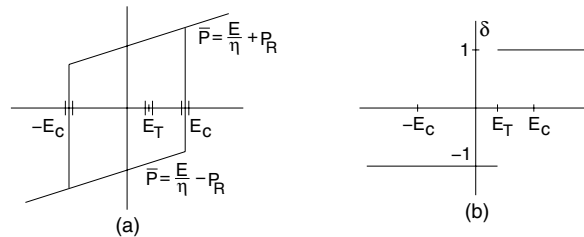


FIG. 14. (a) Points  $E + E_I = -E_c, E_c$ , and  $E_T$  at which  $\delta = \pm 1$  changes sign, and (b) behavior of  $\delta$  associated with the initial dipole distribution at  $E + E_I = E_T$ .

We also note that the decay conditions (12) dictate that  $\nu_1$  and  $\nu_2$  satisfy the relations

$$\begin{aligned} |\nu_2(E_I)| &\leq c_2, \\ \int_{-\infty}^{\infty} \nu_2(E_I) dE_I &\leq b_2, \\ \int_0^{\infty} \nu_1(E_c) dE_c &\leq b_1, \end{aligned}$$

where  $b_1, b_2$ , and  $c_2$  are finite constants.

To establish the continuity of  $P$  with respect to  $E$ , we consider the behavior at field values  $E_0$  and  $E_1$ , where without loss of generality we take  $E_0 < E_1$ . When integrating with respect to  $E_I$ , we decompose the interval  $(-\infty, \infty)$  into seven regions delineated by the points  $-E_c, E_c, E_T$ , as shown in Figure 14(a). For this decomposition, we note that

$$|\bar{P}(E_1 + E_I; E_c, \xi) - \bar{P}(E_0 + E_I; E_c, \xi)| = \begin{cases} \frac{1}{\eta}(E_1 - E_0), & \text{region excludes} \\ & -E_c, E_c, E_T, \\ \frac{1}{\eta}(E_1 - E_0) + 2P_R, & \text{region includes} \\ & -E_c, E_c, E_T. \end{cases}$$

To consolidate notation, we define the integrals

$$\begin{aligned} I(a, b) &= \int_a^b \frac{1}{\eta}(E_1 - E_0) \nu_2(E_I) dE_I, \\ I_{PR}(a, b) &= \int_a^b \left[ \frac{1}{\eta}(E_1 - E_0) + 2P_R \right] \nu_2(E_I) dE_I. \end{aligned}$$

It subsequently follows that

$$\begin{aligned} |P(E_1) - P(E_0)| &\leq \int_0^{\infty} \{ |I(-\infty, -E_c - E_1)| + |I_{PR}(-E_c - E_1, -E_c - E_0)| \\ &\quad + |I(-E_c - E_0, E_T - E_1)| + |I_{PR}(E_T - E_1, E_T - E_0)| \\ &\quad + |I(E_T - E_0, E_c - E_1)| + |I_{PR}(E_c - E_1, E_c - E_0)| \\ &\quad + |I(E_c - E_0, \infty)| \} \nu_1(E_c) dE_c \\ &\leq (E_1 - E_0) \int_0^{\infty} \left\{ \frac{4c_2}{\eta} + 3b_2 \left[ \frac{1}{\eta}(E_1 - E_0) + 2P_R \right] \right\} \nu_1(E_c) dE_c \\ &\leq (E_1 - E_0) b_1 \left( \frac{4c_2}{\eta} + 3b_2 \left[ \frac{1}{\eta}(E_1 - E_0) + 2P_R \right] \right). \end{aligned}$$

For  $\varepsilon > 0$ , take

$$\delta = \min \left\{ \frac{\varepsilon}{b_1 \left( \frac{4c_2}{\eta} + 3b_2 \left[ \frac{1}{\eta}(E_1 - E_0) + 2P_R \right] \right)}, 1 \right\}.$$

Under the assumption that  $E$  is continuous in time and  $E_0 = E(t_0)$ ,  $E_1 = E(t_1)$ , for every  $\delta > 0$  there exists  $\tilde{\delta} > 0$  such that if  $|t_1 - t_0| < \tilde{\delta}$ , we are guaranteed that  $|E_1 - E_0| < \delta$ . It follows that if  $|t_1 - t_0| < \tilde{\delta}$ , the polarization values satisfy the bound

$$|[P(E)](t_1) - [P(E)](t_0)| \leq \varepsilon,$$

thus establishing the continuity of the hysteresis model. This holds for all major and minor loops. As illustrated in Figure 6, the behavior of the model that incorporates thermal activation is smoother than the thermally inactive case considered here. For brevity, we omit the proof of this second case.

## REFERENCES

- [1] B.L. BALL, R.C. SMITH, S-J. KIM, AND S. SEELECKE, *A stress-dependent hysteresis model for ferroelectric materials*, J. Intelligent Material Systems Structures, to appear.
- [2] H.T. BANKS, K. ITO, AND Y. WANG, *Well-posedness for damped second order systems with unbounded input operators*, Differential Integral Equations, 8 (1995), pp. 587–606.
- [3] H.T. BANKS, R.C. SMITH, AND Y. WANG, *Smart Material Structures: Modeling, Estimation and Control*, Masson/John Wiley, Paris/Chichester, 1996.
- [4] T.R. BRAUN AND R.C. SMITH, *Efficient implementation algorithms for homogenized energy models*, Continuum Mech. Thermodynamics, 18 (2006), pp. 137–155.
- [5] W. CHEN AND C.S. LYNCH, *A model for simulating polarization switching and AF-F phase changes in ferroelectric ceramics*, J. Intelligent Material Systems Structures, 9 (1998), pp. 427–431.
- [6] W. CHEN AND C.S. LYNCH, *A micro-electro-mechanical model for polarization switching of ferroelectric materials*, Acta Mater., 46 (1998), pp. 5303–5311.
- [7] D. CROFT, G. SHED, AND S. DEVASIA, *Creep, hysteresis, and vibration compensation for piezoactuators: Atomic force microscopy application*, J. Dynamic Systems, Measurement, and Control, 23 (2001), pp. 35–43.
- [8] A. DANIELE, S. SALAPAKA, M.V. SALAPAKA, AND M. DAHLEH, *Piezoelectric scanners for atomic force microscopes: Design of lateral sensors, identification and control*, in Proceedings of the America Control Conference, San Diego, CA, 1999, IEEE Press, Piscataway, NJ, pp. 253–257.
- [9] R.C.H. DEL ROSARIO AND R.C. SMITH, *Spline approximation of thin shell dynamics*, Internat. J. Numer. Methods Engrg., 40 (1997), pp. 2807–2840.
- [10] R.C.H. DEL ROSARIO AND R.C. SMITH, *LQR control of thin shell dynamics: Formulation and numerical implementation*, J. Intelligent Material Systems Structures, 9 (1998), pp. 301–320.
- [11] R. GARCÍA AND R. PÉREZ, *Dynamic atomic force microscopy methods*, Surface Sci. Reports, 47 (2002), pp. 197–301.
- [12] P. GE AND M. JOUANEH, *Modeling hysteresis in piezoceramic actuators*, Precision Engineering, 17 (1995), pp. 211–221.
- [13] R.J. GIESSIBL, *Advances in atomic force microscopy*, Rev. Modern Phys., 75 (2003), pp. 949–983.
- [14] P.K. HANSMA, V.B. ELINGS, O. MARTI, AND C.E. BRACKER, *Scanning tunneling microscopy and atomic force microscopy: Application to biology and technology*, Science, 242 (1988), pp. 209–242.
- [15] A.G. HATCH, *Model Development and Control Design for Atomic Force Microscopy*, Ph.D. Dissertation, Department of Mathematics, North Carolina State University, Raleigh, NC, 2004.
- [16] A.G. HATCH, R.C. SMITH, T. DE, AND M.V. SALAPAKA, *Construction and experimental implementation of a model-based inverse filter to attenuate hysteresis in ferroelectric transducers*, IEEE Trans. Control Systems Technol., to appear.
- [17] L. HUANG AND H.F. TIERSTEN, *An analytic description of slow hysteresis in polarized ferroelectric ceramic actuators*, J. Intelligent Material Systems Structures, 9 (1998), pp. 417–426.
- [18] C.M. LANDIS, *Non-linear constitutive modeling of ferroelectrics*, Current Opinion in Solid State and Materials Sci., 8 (2004), pp. 59–69.
- [19] W. LU, D.-N. FANG, AND K.-C. HWANG, *Nonlinear electric-mechanical behavior and micromechanics modelling of ferroelectric domain evolution*, Acta Mater., 47 (1999), pp. 2913–2926.

- [20] J.A. MAIN, E. GARCIA, AND D.V. NEWTON, *Precision position control of piezoelectric actuators using charge feedback*, J. Guidance, Control, and Dynamics, 18 (1995), pp. 1068–73.
- [21] J.A. MAIN, D. NEWTON, L. MASSENGIL, AND E. GARCIA, *Efficient power amplifiers for piezoelectric applications*, Smart Materials and Structures, 5 (1996), pp. 766–775.
- [22] J.M. NEALIS AND R.C. SMITH,  $\mathcal{H}_\infty$  control design for a magnetostrictive transducer, in Proceedings of the 42nd IEEE Conference on Decision and Control, Maui, HI, 2003, IEEE Press, Piscataway, NJ, pp. 1801–1806.
- [23] J.M. NEALIS AND R.C. SMITH, *Model-based robust control design for magnetostrictive transducers operating in hysteretic and nonlinear regimes*, IEEE Trans. Control Systems Technol., to appear.
- [24] M.B. OZER AND T.J. ROYSTON, *Modeling the effect of piezoceramic hysteresis in structural vibration control*, Smart Structures and Materials 2001, Proc. SPIE 4326, SPIE, Bellingham, WA, 2001, pp. 89–100.
- [25] P.M. PRENTER, *Splines and Variational Methods*, Wiley, New York, 1975.
- [26] J.K. RAYE AND R.C. SMITH, *A temperature-dependent hysteresis model for relaxor ferroelectric compounds*, Proc. SPIE, Smart Structures and Materials 2004, 5383, SPIE, Bellingham, WA, 2004, pp. 1–10.
- [27] G. ROBERT, D. DAMJANOVIC, AND N. SETTER, *Preisach modeling of piezoelectric nonlinearity in ferroelectric ceramics*, J. Appl. Phys., 89 (2001), pp. 5067–5074.
- [28] D. RUGAR, O. ZÜGER, S.T. HOEN, C.S. YANNONI, H.-M. VIETH AND R.D. KENDRICK, *Force detection of nuclear magnetic resonance*, Science, 264 (1994), pp. 1560–1563.
- [29] S. SALAPAKA, A. SEBASTIAN, J.P. CLEVELAND, AND M.V. SALAPAKA, *High bandwidth nanopositioner: A robust control approach*, Rev. Scientific Instruments, 73 (2002), pp. 3232–3241.
- [30] R.C. SMITH, *Smart Material Systems: Model Development*, Frontiers in Appl. Math. 32, SIAM, Philadelphia, PA, 2005.
- [31] R.C. SMITH AND A. HATCH, *Parameter estimation techniques for nonlinear hysteresis models*, in Smart Structures and Materials 2004, Proc. SPIE 5383, SPIE, Bellingham, WA, 2004, pp. 155–163.
- [32] R.C. SMITH, A. HATCH, B. MUKHERJEE, AND S. LIU, *A homogenized energy model for hysteresis in ferroelectric materials: General density formulation*, J. Intelligent Material Systems Structures, 16 (2005), pp. 713–732.
- [33] R.C. SMITH AND C.L. HOM, *Domain wall theory for ferroelectric hysteresis*, J. Intelligent Material Systems Structures, 10 (1999), pp. 195–213.
- [34] R.C. SMITH AND Z. OUNAIES, *A domain wall model for hysteresis in piezoelectric materials*, J. Intelligent Material Systems Structures, 11 (2000), pp. 62–79.
- [35] R.C. SMITH AND M. SALAPAKA, *Model Development for the Positioning Mechanisms in an Atomic Force Microscope*, Internat. Ser. Numer. Math. 143, Birkhäuser, Basel, Switzerland, 2002, pp. 249–269.
- [36] R.C. SMITH AND S. SEELECKE, *An energy formulation for Preisach models*, Proc. SPIE, Smart Structures and Materials 2002, 4693, SPIE, Bellingham, WA, 2002, pp. 173–182.
- [37] R.C. SMITH, S. SEELECKE, M.J. DAPINO AND Z. OUNAIES, *A unified model for hysteresis in ferroic materials*, in Smart Structures and Materials 2003, Proc. SPIE, 5049, SPIE, Bellingham, WA, 2003, pp. 88–99.
- [38] R.C. SMITH, S. SEELECKE, M.J. DAPINO, AND Z. OUNAIES, *A unified framework for modeling hysteresis in ferroic materials*, J. Mech. Phys. Solids, 54, (2005), pp. 46–85.
- [39] R.C. SMITH, S. SEELECKE, Z. OUNAIES, AND J. SMITH, *A free energy model for hysteresis in ferroelectric materials*, J. Intelligent Material Systems Structures, 14 (2003), pp. 719–739.
- [40] S.A. WOLF, D.D. AWSCHALOM, R.A. BUHRMAN, J.M. DAUGHTON, S. VON MOLNÁR, M.L. CHTCHELKANOVA, AND D.M. TEGER, *Spintronics: A spin-based electronics vision for the future*, Science, 294 (2001), pp. 1488–1495.